QUANTUM SENSING

Improving metrology with quantum scrambling

Zeyang Li (李泽阳)[1], Simone Colombo[1], Chi Shu[1,2], Gustavo Velez[1,3], Saúl Pilatowsky-Cameo[4], Roman Schmied[5], Soonwon Choi[4], Mikhail Lukin[2], Edwin Pedrozo-Peñafiel[1], Vladan Vuletić[1]*

Quantum scrambling describes the spreading of information into many degrees of freedom in quantum systems, such that the information is no longer accessible locally but becomes distributed throughout the system. This idea can explain how quantum systems become classical and acquire a finite temperature, or how in black holes the information about the matter falling in is seemingly erased. We probe the exponential scrambling of a multiparticle system near a bistable point in phase space and utilize it for entanglement-enhanced metrology. A time-reversal protocol is used to observe a simultaneous exponential growth of both the metrological gain and the out-of-time-order correlator, thereby experimentally verifying the relation between quantum metrology and quantum information scrambling. Our results show that rapid scrambling dynamics capable of exponentially fast entanglement generation are useful for practical metrology, resulting in a 6.8(4)-decibel gain beyond the standard quantum limit.

Even though all unitary dynamics of quantum systems are in principle reversible, it is extremely challenging in practice to reverse the arrow of time in generic interacting many-body systems. This is because any small perturbations or imperfections in the time-reversed dynamics can lead to highly complicated, nonlocal changes in quantum wave functions, similar to the butterfly effect in chaos theory. Dubbed information scrambling (*1*–*3*), this quantum-mechanical effect gives rise to a variety of unusual phenomena and applications ranging from models of quantum gravity (*4*, *5*) to quantum metrology (*6*). The speed of information scrambling can be quantified by out-of-time-ordered correlators (OTOCs) (*7*, *8*), which constitute a measure of how fast the noncommutativity between two different quantum operations is established (*9*). In certain systems, the OTOC grows exponentially fast over time $e^{\lambda_Q t}$, where $\lambda_Q > 0$ defines the generalized quantum Lyapunov exponent (*8*). OTOCs have been measured (*10*) and used as probes for various many-body phenomena, such as thermalization (*11*), quantum phase transitions (*12*), many-body entanglement growth (*13*), and quantum scrambling (*14*–*16*). However, the observation of exponential scrambling has remained elusive.

One approach to effective time reversal involves changing the sign of the Hamiltonian $\hat{H} \rightarrow -\hat{H}$ during the evolution of highly engineered quantum systems. In the field of quantum metrology, this enables a family of powerful quantum amplification protocols (*17*–*24*) such as signal amplification through time-reversed interaction (SATIN) (*23*). Such protocols can be robust against many limitations that usually affect entanglement-enhanced atomic sensors, including imperfect measurements. In the presence of exponential scrambling dynamics (Fig. 1A), the SATIN signal is also amplified exponentially over time.

Experimental setup

The Lipkin-Meshkov-Glick (LMG) Hamiltonian (*24*, *25*–*34*) is of particular interest in this context, as it exhibits exponential evolution in phase space while it can be experimentally realized in a cavity quantum electrodynamics (cQED) system. The latter is accomplished by adding a global rotation term $\hat{S}_x$ to the one-axis-twisting (OAT) (*35*) Hamiltonian $\hat{S}_z^2$

$$\hat{H} = \chi \hat{S}_z^2 + \Omega \hat{S}_x \quad (1)$$

Here $S = (\hat{S}_x, \hat{S}_y, \hat{S}_z)$ represents the total spin of the system consisting of $N = 2S$ spin-$\frac{1}{2}$ particles, χ is the shearing parameter for OAT, and Ω is the transverse rotation frequency. Although the time evolution is not chaotic because of the conservation of $\hat{S}^2$, the LMG Hamiltonian nevertheless features a quantum Lyapunov exponent for $0 < \Omega/(S\chi) < 2$ due to an unstable (bifurcating) trajectory in the system phase space (Fig. 1A) (*32*, *36*, *37*).

Our experiments operate with $N = 200$ ^{171}Yb atoms whose magnetic sublevels $|\uparrow, \downarrow\rangle$ in the electronic ground state represent a spin-$\frac{1}{2}$ system. One of the two spin states ($|\uparrow\rangle$) couples to an electronically excited state $|e\rangle$ via σ^+-polarized light that circulates inside the optical cavity (Fig. 1B). The coupling between a single atom and the cavity is characterized by the single-atom cooperativity $\eta = 8.8(2)$ (*38*). We implement the LMG Hamiltonian in the rotating frame by adding an oscillating transverse magnetic field to the OAT Hamiltonian (*34*) [Fig. 1B and supplementary materials (SM) (*39*)].

The experiments start by initializing the system in a coherent spin state (CSS) pointing along the x axis by means of optical pumping followed by a $\pi/2$ spin rotation. Analytical solutions using the Holstein-Primakoff approximation (*40*) show that for $\Omega/(S\chi) < 0$ or $\Omega/(S\chi) > 2$, the system evolution is periodic with a frequency $\omega = \sqrt{\Omega^2 - 2S\chi\Omega}$ (*41*). However, for $0 < \Omega/(S\chi) < 2$ the frequency ω becomes imaginary, corresponding to an

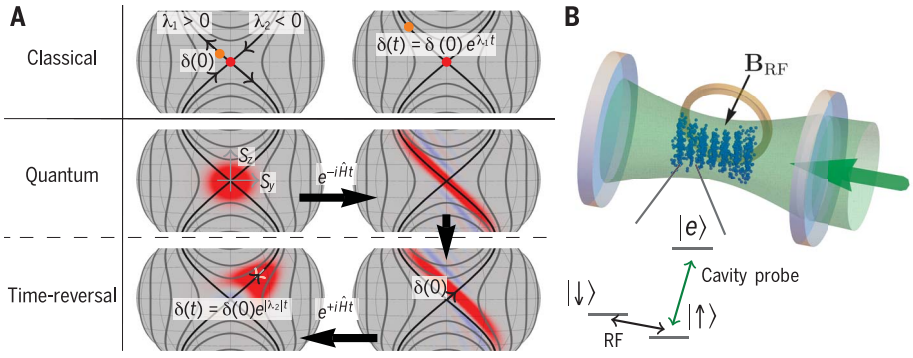

Fig. 1. Time-reversal–based exponential growth of sensitivity in a system with an unstable fixed point. (**A**) Classically, for a trajectory with a positive Lyapunov exponent $\lambda_1 > 0$, an initial signal (displacement) $\delta(0)$ increases exponentially over time. For quantum dynamics, however, an initial overlap between two states is preserved under unitary evolution. To amplify the signal similarly to the classical case, one needs to evolve the state under the nonlinear $\hat{H}$, resulting in decreased quantum fluctuations along a direction with negative Lyapunov coefficient $\lambda_2 < 0$. A displacement along this direction followed by application of the negative Hamiltonian $-\hat{H}$ (such that $\lambda_{1,2} \rightarrow -\lambda_{1,2}$) is then used to amplify the signal. The plots represent the evolution on the Bloch sphere, where the S_y and S_z axes are labeled as in the left subplot of the middle row. (**B**) Experimental setup. The LMG Hamiltonian is generated by the interaction of the collective atomic spin with light inside a cavity on the transition $|\uparrow\rangle \rightarrow |e\rangle$, while a radiofrequency magnetic field is applied to rotate the atomic spin.

[1]Department of Physics, MIT-Harvard Center for Ultracold Atoms, Research Laboratory of Electronics, Massachusetts Institute of Technology, Cambridge, MA 02139, USA. [2]Department of Physics, Harvard University, Cambridge, MA 02138, USA. [3]Department of Electrical Engineering and Computer Science, Massachusetts Institute of Technology, Cambridge, MA 02139, USA. [4]Department of Physics, Massachusetts Institute of Technology, Cambridge, MA 02139, USA. [5]Viewpointsystem GmbH, 1010 Wien, Austria.
*Corresponding author. Email: vuletic@mit.edu

unstable-fixed-point exponential evolution with a Lyapunov exponent $\lambda_Q = |\omega|$. For a fixed $S\chi$, choosing $\Omega = S\chi$ results in a maximum Lyapunov exponent $\lambda_Q = |S\chi|$.

Metrological gain

We first measure the antisqueezing {largest variance $\xi_+^2 \equiv \max_\alpha[\mathrm{var}(S_\alpha)]/(S/2)$} of the collective spin S after an evolution under $\hat{H}$ as a function of the ratio $\Omega/(S\chi)$. The antisqueezing ξ_+ constitutes an upper bound on the quantum Fisher information (QFI) with respect to spin rotations (*42*). As shown in Fig. 2B, the experimental data for ξ_+^2 agree with the numerical simulation of the model (solid red line) and show a peak at $\Omega = S\chi$, as expected.

We then measure in Fig. 2C how ξ_+^2 grows with time for the two cases $\Omega = 0$ (OAT Hamiltonian) and $\Omega = S\chi$ (critically tuned LMG Hamiltonian). The OAT data (gray) exhibit quadratic growth of ξ_+^2, as expected. The LMG data (red) show exponential growth of $\xi_+^2 = e^{2\lambda_Q t}$, with $\lambda_Q = S\chi$ for times $t \lesssim (S\chi)^{-1}$. For larger times, the growths slows because of finite particle number and light-induced decoherence (*34*, *39*). The finite total spin further causes the states to turn non-Gaussian, which we characterize via the Binder cumulant (*43*) (Fig. 2D).

The time evolution under the critically tuned ($\Omega = S\chi$) LMG Hamiltonian $\hat{H}$ quickly prepares an entangled collective quantum state. To implement quantum metrology with the SATIN protocol, we then apply a small rotation $\hat{U}_{\delta\phi} = e^{-i\hat{S}_\alpha \delta\phi}$, where $\hat{S}_\alpha \equiv \hat{S}_y \cos\alpha + \hat{S}_z \sin\alpha$ represents a collective spin operator in the yz plane. This encodes a signal phase $\delta\phi$ along the α direction, with $\alpha = \pi/4$ chosen to maximize the metrological gain [Fig. 1A and SM (*39*)]. To implement $-\hat{H}$, we switch to another set of laser frequencies incident on the cavity and flip the sign of the transverse field Ω [SM (*39*)]. This generates an effective backward evolution in time that amplifies the applied signal $\delta\phi$. The shifted state then undergoes a bifurcated trajectory for $\delta\phi \lesseqgtr 0$ (see Fig. 2C), resulting in an exponentially amplified deviation $G\delta\phi$ from the original position. We measure the mean spin value $\langle \hat{S}_\alpha \rangle = S\sin(G\delta\phi)$ to infer the signal amplification G. As shown in Fig. 3, the squared signal amplification G^2 (orange) increases exponentially with the same exponent $2\lambda_Q$ as the antisqueezing ξ_+^2 up to times $t \approx (S\chi)^{-1}$. The measured quantum noise N^2, i.e., the variance of spin projection noise along the amplification direction $\hat{S}_\alpha$ normalized to the standard quantum limit (SQL) (blue), remains unity until $t \approx 0.8(S\chi)^{-1}$. The subsequent increase of the noise N^2 results from the residual light-atom entanglement (*34*) and can be improved in the future by optimizing the light detuning (*39*). The improvement of the metrological gain over the SQL is 6.8(4) dB.

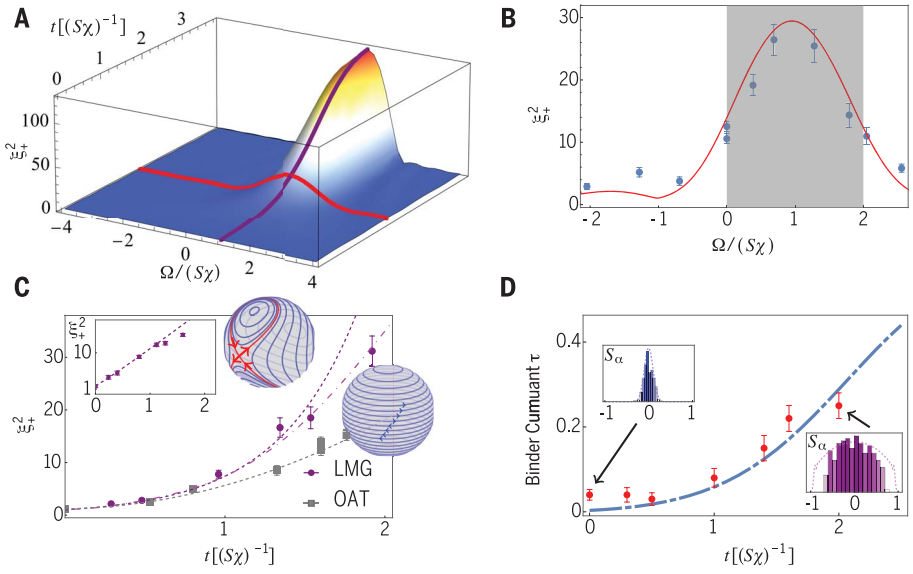

Fig. 2. Collective-spin evolution in the cQED system. (**A**) Numerical calculation of the normalized variance ξ_+^2 of the antisqueezed direction as a function of $S\chi t$ and $\Omega/S\chi$ with linecuts representing the measurements in (B) and (C). (**B**) Experimentally measured antisqueezing (blue symbols) and theoretical expectation (red line) for $S\chi t = 1.8$ as a function of the rotation strength Ω. The shaded region indicates exponential growth, whereas in the other regions the time evolution is either quasi-periodic or growing polynomially. (**C**) Comparison of antisqueezing ξ_+^2 between the fastest exponential growth for a critical rotation strength $\Omega = S\chi$, and the polynomial growth of pure OAT ($\Omega = 0$). The two Bloch spheres represent the lines of classical evolution in both situations. The dashed and dash-dotted red lines represent exponential growth based on the theoretically predicted Lyapunov exponent and the full numerical result, respectively, with no free parameters. The gray dashed line is calculated for $\Omega = 0$. (Inset) Logarithmic plot for $\Omega = S\chi$ showing the exponential growth of ξ_+^2. (**D**) The Binder cumulant B (characterizing the deviation from a Gaussian distribution for $B > 0$) for the antisqueezed direction for the critical LMG condition $\Omega = S\chi$ versus time t. (Insets) Measured spin distributions for $S\chi t = 0$ (blue) and $S\chi t = 2$ (purple), with the latter being strongly non-Gaussian.

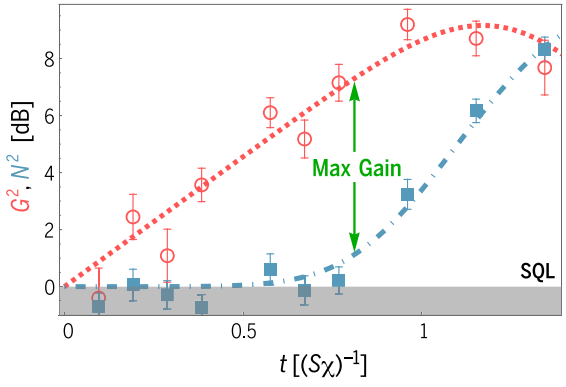

Fig. 3. Metrological gain with exponential LMG time-reversal protocol. The squared signal amplification G^2 (pink open circles) and system noise N^2 (blue solid squares) versus time t. The pink dashed line represents the exponential growth of the antisqueezing shown in Fig. 2, and constitutes an upper bound to the QFI. The blue dash-dotted line is the calculated noise (with no free parameters) due to residual light-atom entanglement. The maximum metrological gain is 6.8(4) dB.

The deviation of G^2 from an exponential for $t \gtrsim (S\chi)^{-1}$ is due to the nonuniform coupling between atoms and the cavity light (*44*), as well as the residual light-atom entanglement, both of which can be improved in the future (*34*, *45*).

Quantum metrology and quantum information

To investigate the quantum information science aspect of the time-reversal protocol, we measure the fidelity OTOC (FOTOC) with quantum state tomography using randomized measurements (*39*, *46*, *47*). The FOTOC $\mathcal{F}(t)$ can be expressed as the trace between the density matrix $\rho(0)$ of the original state and that of the state displaced by $\delta\phi$ evolved backward in time, $\rho'_t(0) := \hat{U}_t \hat{\rho}(0) \hat{U}_t^\dagger$, where $\hat{U}_t := e^{i\hat{H}t} e^{-i\hat{S}_\alpha \delta\phi} e^{-i\hat{H}t}$

$$\mathcal{F}(t) \equiv \left\langle \hat{U}_t \hat{\rho}(0) \hat{U}_t^\dagger \hat{\rho}(0) \right\rangle = Tr\left(\rho'_t(0)\rho(0)\right) \quad (2)$$

At fixed forward evolution time t, the FOTOC $\mathcal{F}$ depends on the small displacement $\delta\phi$ and

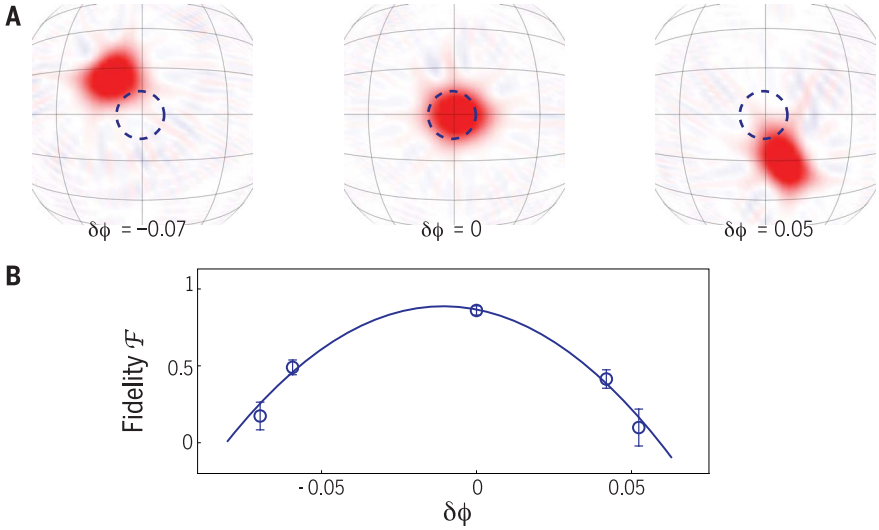

Fig. 4. FOTOC and OTOC extracted from quantum state tomography. (**A**) Experimental Wigner functions obtained from quantum state tomography after applying the LMG SATIN protocol with different signal displacements $\delta\phi$ [for $\Omega = S\chi$ and $t = 0.57(S\chi)^{-1}$]. The dashed circle indicates the original CSS state. (**B**) The solid blue line is a quadratic fit to the data (open circles), used to extract the OTOC $\mathcal{I}$ (see text and Eq. 3).

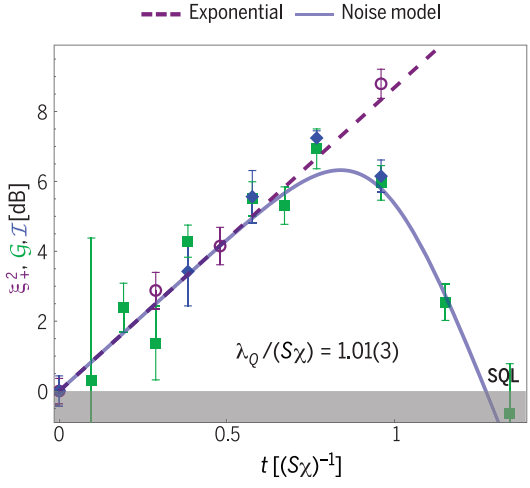

Fig. 5. Comparison between quantum information and quantum metrology parameters for the LMG model. The purple open circles, solid green squares, and solid blue diamonds represent the antisqueezing, metrological gain, and OTOC, respectively. All quantities increase initially exponentially with time with a fitted Lyapunov exponent $\lambda_Q = 1.01(3)S\chi$ that agrees well with the theoretical prediction $\lambda_Q = S\chi$. The OTOC error bars are obtained by using the bootstrapping method (*39*, *50*). For longer times $t \gtrsim (S\chi)^{-1}$, the metrological gain and OTOC decrease owing to decoherence caused by light-atom entanglement, as is well captured by the theoretical model (solid blue line) without free parameters.

is related to the OTOC $\mathcal{I}(t)$ by its second derivative (*12*)

$$\mathcal{I}(t) \equiv -\frac{1}{2}\frac{\partial^2 \mathcal{F}(t)}{(\partial\delta\phi)^2}\bigg|_{\delta\phi=0} = \left\langle \hat{S}_\alpha(t)\hat{\rho}(0)\hat{S}_\alpha(t)\hat{\rho}(0)\right\rangle \quad (3)$$

with the Hermitian operator $\hat{S}_\alpha(t) := e^{i\hat{H}t}\hat{S}_\alpha e^{-i\hat{H}t}$.

Choosing four different evolution times (such that $S\chi t_1 \in \{0.38, 0.57, 0.77, 0.96\}$), we displace the entangled state for each t_1 by several different small angles $\delta\phi$. We then perform the tomographic reconstruction after a reversed time evolution with $-\hat{H}$ to obtain $\mathcal{F}(t_1)$, as shown in Fig. 4A. The OTOC $\mathcal{I}(t_1)$ is then extracted from the data by fitting a quadratic function in the displacement $\delta\phi$ to the FOTOC (Fig. 4B). We notice that the fitted quadratic curve is slightly shifted from $\delta\phi = 0$ and has slightly reduced peak fidelity. The shift is likely due to a small difference between the assumed and actual Larmor frequencies between the spin states, whereas the reduction from unit peak fidelity is due to the imperfect time reversal associated with residual light-atom entanglement. The small imperfections do not reduce the metrological gain appreciably (*39*).

Figure 5 summarizes our findings regarding the close relation between quantum scrambling and time-reversal quantum metrology: The antisqueezing ξ_+^2, metrological gain $\mathcal{G} := G^2/N^2$, and OTOC $\mathcal{I}$ all agree with each other and scale exponentially with application time t of the LMG Hamiltonian for $t \lesssim 0.8(S\chi)^{-1}$. The exponential fit yields a Lyapunov exponent $\lambda_Q/(S\chi) = 1.01 \pm 0.03$, in excellent agreement with the theoretical expectation $\lambda_Q/(S\chi) = 1$.

Concluding remarks

Our experiments demonstrate a cQED realization of the critically tuned ($\Omega = S\chi$) LMG model with an exponential evolution in phase space. We also point out and experimentally verify that time-reversal protocols represent a powerful experimental tool giving access not only to metrological gain beyond the SQL (*22*, *23*, *48*), but also enabling the measurement of quantum information scrambling in many-body systems. This generalizes the possibilities of using quantum information science to enhance quantum metrology (*49*). Furthermore, we observe exponential growth of both the OTOC and the metrological gain for the LMG model, thereby experimentally verifying the intrinsic relation between these two concepts from different subfields of quantum science. The demonstrated methods to reverse time evolution may enable the experimental investigation of complex many-body quantum systems in which the information spreads exponentially fast within many degrees of freedom.

REFERENCES AND NOTES

1. Y. Sekino, L. Susskind, *J. High Energy Phys.* **2008**, 065 (2008).
2. B. Swingle, G. Bentsen, M. Schleier-Smith, P. Hayden, *Phys. Rev. A* **94**, 040302 (2016).
3. R. J. Lewis-Swan, A. Safavi-Naini, J. J. Bollinger, A. M. Rey, *Nat. Commun.* **10**, 1581 (2019).
4. T. Schuster *et al.*, *Phys. Rev. X* **12**, 031013 (2022).
5. S. Nezami *et al.*, *PRX Quantum* **4**, 010321 (2023).
6. J. Appel *et al.*, *Proc. Natl. Acad. Sci. U.S.A.* **106**, 10960–10965 (2009).
7. A. Larkin, Y. N. Ovchinnikov, *Sov. Phys. JETP* **28**, 1200 (1969).
8. A. Kitaev, A simple model of quantum holography [video] (2015). https://online.kitp.ucsb.edu/online/entangled15/kitaev/. See also J. Maldacena, D. Stanford, *Phys. Rev. D* **94**, 106002 (2016).
9. I. García-Mata, R. A. Jalabert, D. A. Wisniacki, *Scholarpedia* **18**, 55237 (2023).
10. J. Li *et al.*, *Phys. Rev. X* **7**, 031011 (2017).
11. A. M. Green *et al.*, *Phys. Rev. Lett.* **128**, 140601 (2022).
12. K. X. Wei *et al.*, *Phys. Rev. Lett.* **123**, 090605 (2019).
13. M. Gärttner *et al.*, *Nat. Phys.* **13**, 781–786 (2017).
14. K. A. Landsman *et al.*, *Nature* **567**, 61–65 (2019).
15. J. Braumüller *et al.*, *Nat. Phys.* **18**, 172–178 (2022).
16. X. Mi *et al.*, *Science* **374**, 1479–1483 (2021).
17. E. Davis, G. Bentsen, M. Schleier-Smith, *Phys. Rev. Lett.* **116**, 053601 (2016).
18. F. Fröwis, P. Sekatski, W. Dür, *Phys. Rev. Lett.* **116**, 090801 (2016).
19. O. Hosten, R. Krishnakumar, N. J. Engelsen, M. A. Kasevich, *Science* **352**, 1552–1555 (2016).
20. S. P. Nolan, S. S. Szigeti, S. A. Haine, *Phys. Rev. Lett.* **119**, 193601 (2017).
21. T. Macrì, A. Smerzi, L. Pezzè, *Phys. Rev. A* **94**, 010102 (2016).
22. K. A. Gilmore *et al.*, *Science* **373**, 673–678 (2021).
23. S. Colombo *et al.*, *Nat. Phys.* **18**, 925–930 (2022).
24. T.-W. Mao *et al.*, Quantum enhanced sensing by echoing spin-nematic squeezing in atomic Bose-Einstein condensate (2022). arXiv:2212.09124.
25. H. J. Lipkin, N. Meshkov, A. Glick, *Nucl. Phys.* **62**, 188–198 (1965).

26. L.-M. Duan, A. Sørensen, J. I. Cirac, P. Zoller, *Phys. Rev. Lett.* **85**, 3991–3994 (2000).
27. T. Zibold, E. Nicklas, C. Gross, M. K. Oberthaler, *Phys. Rev. Lett.* **105**, 204101 (2010).
28. C. D. Hamley, C. Gerving, T. Hoang, E. Bookjans, M. S. Chapman, *Nat. Phys.* **8**, 305–308 (2012).
29. H. Strobel *et al*., *Science* **345**, 424–427 (2014).
30. W. Muessel *et al*., *Phys. Rev. A* **92**, 023603 (2015).
31. J. Peise *et al*., *Nat. Commun.* **6**, 8984 (2015).
32. S. Pilatowsky-Cameo *et al*., *Phys. Rev. E* **101**, 010202 (2020).
33. J. A. Muniz *et al*., *Nature* **580**, 602–607 (2020).
34. Z. Li *et al*., *PRX Quantum* **3**, 020308 (2022).
35. M. Kitagawa, M. Ueda, *Phys. Rev. A* **47**, 5138–5143 (1993).
36. S. Pappalardi *et al*., *Phys. Rev. B* **98**, 134303 (2018).
37. E. B. Rozenbaum, L. A. Bunimovich, V. Galitski, *Phys. Rev. Lett.* **125**, 014101 (2020).
38. H. Tanji-Suzuki *et al*., in *Advances in Atomic, Molecular, and Optical Physics*, E. Arimondo, P. R. Bermna, C. C. Lin, Eds. (Academic Press, 2011), vol. 60, pp. 201–237.
39. See supplementary materials for details.
40. T. Holstein, H. Primakoff, *Phys. Rev.* **58**, 1098–1113 (1940).
41. C. K. Law, H. T. Ng, P. T. Leung, *Phys. Rev. A* **63**, 055601 (2001).
42. L. Pezzè, A. Smerzi, M. K. Oberthaler, R. Schmied, P. Treutlein, *Rev. Mod. Phys.* **90**, 035005 (2018).
43. K. Binder, *Z. Phys. B Condens. Matter Quanta* **43**, 119–140 (1981).
44. J. Hu, W. Chen, Z. Vendeiro, H. Zhang, V. Vuletić, *Phys. Rev. A* **92**, 063816 (2015).
45. B. Wu, G. P. Greve, C. Luo, J. K. Thompson, Site-dependent selection of atoms for homogeneous atom-cavity coupling. arXiv:2104.01201 [quant-ph] (2021).
46. R. Schmied, P. Treutlein, *New J. Phys.* **13**, 065019 (2011).
47. A. Elben *et al*., *Nat. Rev. Phys.* **5**, 9–24 (2023).
48. D. Barberena, S. R. Muleady, J. J. Bollinger, R. J. Lewis-Swan, A. M. Rey, Fast generation of spin squeezing via resonant spin-boson coupling. arXiv:2201.10622 [quant-ph] (2022).
49. C. D. Marciniak *et al*., *Nature* **603**, 604–609 (2022).
50. W. Hardle, J. S. Marron, *Ann. Stat.* **19**, 778 (1991).
51. Z. Li *et al*., Improving metrology with quantum scrambling, *Dryad*, dataset (2023). https://doi.org/10.5061/dryad.zkh1893fj.

ACKNOWLEDGMENTS

We thank J. Thompson, M. Schleier-Smith, B. Braverman, and A. Adiyatullin for inspiring discussions. We also thank M. Liu for helping resolve the subtleties of using bootstrap method to extract statistical uncertainties. **Funding:** We acknowledge financial support from ONR (grant N00014-20-1-2428), the National Science Foundation through the Center for Ultracold Atoms (grant PHY-1734011) and NSF QLCI (Award OMA - 2016244), DOE QSA (through grant DE-SC0021013 and LBNL QSA Center), and ARO (grant W911NF1910517). **Author contributions:** Z.L., S. Colombo, C.S., G.V., and E.P. contributed to building the experimental setup and performed the measurements. Z.L. and S.Colombo analyzed the data, numerically simulated the experiments, and contributed to theoretical interpretation of the results. R.S. contributed to developing the quantum state tomography method. S.P.-C. and S. Choi contributed to the theoretical interpretation of the results. All work was supervised by V.V. All authors discussed the results and contributed to the manuscript. **Competing interests:** The authors declare no competing interests. **Data and materials availability:** All data needed to evaluate the conclusions in the paper are present in the figures of the paper and/or the supplementary materials. The data can be accessed at Dryad (*51*).

SUPPLEMENTARY MATERIALS

science.org/doi/10.1126/science.adg9500
Materials and Methods
Figs. S1 and S2
Tables S1 and S2
References (*52*–*58*)

Submitted 1 February 2023; accepted 19 May 2023
10.1126/science.adg9500